# Quantitative phase-field lattice-Boltzmann study of lamellar eutectic growth under natural convection

A. Zhang,[1] Z. Guo,[1,*] and S.-M. Xiong[1,2,†]

[1]*School of Materials Science and Engineering, Tsinghua University, Beijing 100084, People's Republic of China*

[2]*Key Laboratory for Advanced Materials Processing Technology, Ministry of Education, Tsinghua University, Beijing 100084, People's Republic of China*

(Received 19 October 2017; revised manuscript received 19 February 2018; published 2 May 2018)

The influence of natural convection on lamellar eutectic growth was determined by a comprehensive phase-field lattice-Boltzmann study for Al-Cu and $CBr_4$-$C_2Cl_6$ eutectic alloys. The mass differences resulting from concentration differences led to the fluid flow and a robust parallel and adaptive mesh refinement algorithm was employed to improve the computational efficiency. By means of carefully designed "numerical experiments", the eutectic growth under natural convection was explored and a simple analytical model was proposed to predict the adjustment of the lamellar spacing. Furthermore, by alternating the solute expansion coefficient, initial lamellar spacing, and undercooling, the microstructure evolution was presented and compared with the classical eutectic growth theory. Results showed that both interfacial solute distribution and average curvature were affected by the natural convection, the effect of which could be further quantified by adding a constant into the growth rule proposed by Jackson and Hunt [Jackson and Hunt, Trans. Metall. Soc. AIME **236**, 1129 (1966)].

DOI: 10.1103/PhysRevE.97.053302

## I. INTRODUCTION

The presence of melt convection could greatly alter the eutectic microstructure patterns during solidification, which has been extensively studied since the pioneering work by Jackson and Hunt [1–6]. It is well accepted that the flow (due to convection) changes the eutectic morphology by altering local solute and/or thermal distribution in the melt [7–9].

There are mainly two types of convection occurring during the directional solidification, including the forced convection caused by imposed external fields (e.g., stir or electromagnetic field) and the natural convection driven by the solute (or density) and/or thermal difference. The former has been preliminarily studied by assuming a constant flow velocity gradient $G_u$ along the growth direction, as designated by the dashed red lines in Fig. 1, in which a transverse flow is assumed perpendicular to the lamellae [2–4]. The steady-state solute field $C(x, y)$ ahead of the assumed planar solid/liquid (S/L) interface is controlled by the following equation.

$$D_L \nabla^2 C + V \frac{\partial C}{\partial y} - y G_u \frac{\partial C}{\partial x} = 0, \tag{1}$$

where $D_L$ is the liquid solute diffusivity and $V$ is the growth velocity. The coordinate system $(x, y)$ is defined and shown in Fig. 1, in which $y$ denotes the distance away from the S/L interface and $x$ starts from the midpoint of the $\alpha$/L interface. However, for the natural convection, related studies are significantly limited. Ma *et al.* [4] proposed an approximate solution of Eq. (1) under the assumption of weak convection, and extended their results to the natural convection case. By assuming a heated vertical flat plate in a semi-infinite body of liquid, they found that the lamellar spacing under natural convection would increase with increasing Grashof number, and their result was qualitatively consistent with that by Baskaran and Wilcox [3].

However, in Eq. (1), the flow parallel to the lamellae was actually neglected, which was inappropriate for natural convection. The fluid flow driven by the solute (or density) difference will form semicircular streamlines with the triple point as the center (see the dashed blue lines in Fig. 1) [10]. Furthermore, related experiments on Al-Cu alloys by Lee *et al.* [5] indicated that for eutectic and near-eutectic alloys, the lamellar spacing would not have noticeable variations, but in nearly all available studies, attention was focused on the effect of convection on lamellar spacing, which mostly disagreed with experiments [5] and neglected the microstructure evolution (e.g., the lamellar width adjustment of coexisting solid phases). Therefore, a more quantitative study is required to precisely elucidate how natural convection affects eutectic growth. Considering that there are many uncertainties in experiments, numerical simulation has become an indispensable way to reproduce the interaction of multiphysical fields during solidification. Wang *et al.* [11] performed a Monte Carlo simulation of eutectic growth with weak convection and found that the convection induced more scattered lamellar spacing. Siquieri and Emmerich [12] simulated the eutectic growth with convection by coupling the Navier-Stokes equations into the phase-field equations, and found that the convection would change the lamellar spacing predicted by the Jackson-Hunt theory and lamellar growth direction. Besides that, to our best knowledge, there have been very limited numerical studies to investigate the effect of convection on eutectic growth.

The numerical solution of the eutectic growth under natural convection comprises two modules: solution of eutectic phase

*zhipeng_guo@mail.tsinghua.edu.cn

†smxiong@tsinghua.edu.cn

 

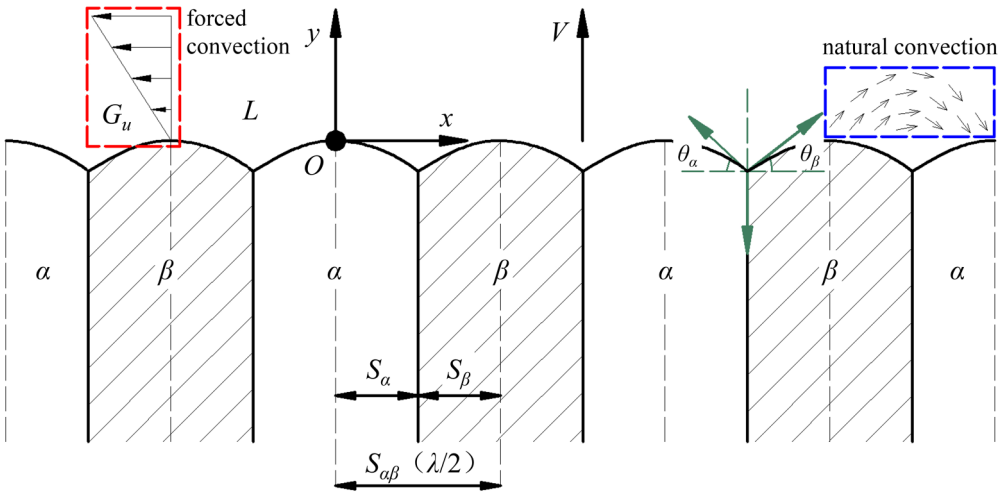


FIG. 1. Schematic illustration of lamellar eutectic growth with convection.

transition and calculation of coupled flow field. Great progress has been made for the former case via phase-field modeling [13–15]. For the latter, however, the conventional macroscopic continuum-based Navier-Stokes (NS) solvers are significantly limited in handling the discontinuity of flow velocity near the moving S/L interface [16]. Beckermann *et al.* [17] first performed coupled solute-convection phase-field study by assuming that the solid phase was rigid and stationary. Tong *et al.* [18] adopted the multigrid SIMPLE method to solve NS equations during phase-field simulations of dendritic growth. The current authors [19,20] employed a parallel-multigrid approach to solve the conservation equations for flow when simulating the dendritic growth with coupled multiphysical fields. In all these numerical models, the solving process of NS equations is rather complex and enormously time consuming. Sun *et al.* [16] found that if the solid fraction was larger than 30%, the simulation would not converge due to the increasingly complicated microstructure morphologies.

As a more appreciable approach, the lattice-Boltzmann method (LBM) has emerged with great potential to solve energy, momentum, and mass transport problems by relaxation to a local equilibrium [21]. The scheme is especially prosperous in fluid flows encompassing interfacial dynamics and complex boundaries with its attractive advantages of good stability and high computational performance [16,22]. Several attempts have been successfully combined with phase-field models to simulate the dendritic growth with liquid convection [23–26]. Therefore, it seems reasonable to couple the LBM into the eutectic phase-field models to retrieve the interaction of eutectic microstructure and fluid flow.

Although the phase-field method has been extensively employed in primary [27–32] and eutectic [15,33–35] phase transitions with its thermodynamic rigor [36–38], efficient solution of the strongly coupled governing equations is still a major challenge [39]. Several attempts have been developed to tackle the practical difficulties during the phase-field simulation of eutectic growth, such as adopting simplified models [40], setting the threshold to exclude the bulk phases [41,42] and a moving window technique [43,44]. To efficiently tackle this practical difficulty, the current authors [35,45,46] developed a robust parallel-adaptive mesh refinement (para-AMR) algorithm to recover the underlying physics without compromising any accuracy. Results showed that this approach could improve the computational efficiency by two to three orders of magnitude.

In this work, we coupled the LBM with the para-AMR algorithm to study the effect of natural convection on the eutectic growth. In particular, the phase-field model was employed to simulate eutectic evolution while the LBM was to simulate the melt flow. Through carefully designed "numerical experiments", the eutectic growth under natural convection was explored and a simple analytical model was proposed to predict the adjustment of the lamellar spacing. Moreover, several key mechanisms of eutectic growth were highlighted and compared with the classical theory proposed by Jackson and Hunt [1].

## II. METHODS

In real cases, the thermal diffusivity is normally three to five orders of magnitude larger than the liquid solute diffusivity, and accordingly the thermal diffusion inside the domain could be neglected [26]. A two-dimensional (2D) isothermal solidification under the low-undercooling condition was assumed in the present simulations. The computational domain was a square filled with supercooled melt, in which four lamellar couples were set at the bottom. To reproduce an infinite melt reservoir, a periodic boundary condition was imposed along the direction perpendicular to the growth direction for all variables including phase field, solute, and flow. For the bottom and top sides, a zero Neumann condition was applied for phase field and solute, while a no-slip boundary condition was for flow. The natural convection was induced by the concentration difference, and the velocity near the diffusion interface was determined by additional dissipative forces to recover the sharp-interface limit [17,18].

### A. Phase-field model

The phase-field model proposed by Kim *et al.* [33] was extended by coupling the melt convection into the diffusion equation [see Eq. (4)] (note that the phase field is not convective

[12,18]). By introducing three order parameters $\phi_1$, $\phi_2$, and $\phi_3$ to designate the liquid phase ($L$) and two solid phases ($\alpha$ and $\beta$), the energy functional $F$ and corresponding governing equations become

$$F = \int_V \left[ \sum_{j>i} \sum_i \left( -\frac{\varepsilon_{ij}^2}{2} \nabla\phi_i \cdot \nabla\phi_j + \omega_{ij}\phi_i\phi_j \right) + \sum_i \phi_i f^i(C_i) + \lambda_L \left( \sum_i \phi_i - 1 \right) \right] dV, \quad (2)$$

$$\frac{\partial \phi_i}{\partial t} = -\frac{2}{n} \sum_{j\neq i}^{n} s_i s_j M_{ij} \left( \frac{\delta F}{\delta \phi_i} - \frac{\delta F}{\delta \phi_j} \right), \quad (3)$$

$$\frac{\partial C}{\partial t} + \phi_3 \vec{v} \cdot \nabla C = \nabla \cdot D \sum_i \phi_i \nabla C_i, \quad (4)$$

where the coexisting three phases $\phi_i$ ($i = 1, 2, 3$) vary between 0 and 1, and maintain the sum to be 1 at any position of the system, e.g., $\phi_3 = 1$ and $\phi_1 = \phi_2 = 0$ in the $L$ phase. $f^i(C_i)$ is the free energy density of the $i$ phase with concentration $C_i$, $\lambda_L$ is the corresponding Lagrange multiplier, $\varepsilon_{ij}$ is the gradient energy coefficient, $\omega_{ij}$ is the height of the double well potential, and $s_i$ is a step function, i.e., $s_i(x,t) = 0$ if $\phi_i = 0$ and $s_i(x,t) = 1$ otherwise. $M_{ij}$ is the phase-field mobility and is determined by assuming a vanishing kinetic effect during solidification. The concentration of the coexisting phases is determined by a weighted average, i.e., $C(x,t) = \sum_i \phi_i C_i$. $\vec{v}$ is the intrinsic flow velocity induced by the concentration difference, which is expanded as $\vec{v} = (u, v)$ in the 2D case and calculated using the LBM. $D$ is the diffusivity dependent on the phase field, i.e., $D = \phi_3 D_L + (1 - \phi_3) D_S$, where $D_S$ is the solute diffusivity in the solid phase. More details including the parameters of the eutectic model and the discretization of the phase-field equations can be found elsewhere [33,35,45].

### B. Lattice-Boltzmann model

As a mesoscopic kinetic-based approach, the LBM assumes that the flow field comprises a series of pseudoparticles represented by a distribution function [47]. The macroscopic flow is characterized by the streaming and collision of these particles. A generally employed approximation of the Boltzmann equations is the Bhatnagar-Gross-Krook (BGK) approach [48], in which the collision term is expressed by a single relaxation time scheme. In this lattice BGK (LBGK) model, the local equilibrium distribution is chosen to recover the NS equations by the Chapman-Enskog analysis [49,50].

In the current 2D case, a so-called two-dimensional nine-velocity (D2Q9) model was employed to calculate the isothermal incompressible flow. The discrete velocities $\vec{c}_i$ along nine different directions are defined as

$$\vec{c}_i = \begin{cases} (0,0) & i = 0 \\ c\left\{\cos\left[(i-1)\frac{\pi}{2}\right], \sin\left[(i-1)\frac{\pi}{2}\right]\right\} & i = 1,2,3,4, \\ \sqrt{2}c\left\{\cos\left[(2i-1)\frac{\pi}{4}\right], \sin\left[(2i-1)\frac{\pi}{4}\right]\right\} & i = 5,6,7,8 \end{cases} \quad (5)$$

where $c = \delta x/\delta t$ is the lattice velocity; $\delta x$ is the lattice spacing, equal for both directions; and $\delta t$ is the time step. Note that both $\delta x$ and $\delta t$ are formally rescaled to 1, which are different from those (i.e., $\Delta x$ and $\Delta t$) in the phase-field part though they are actually the same "material" quantities [25]. The evolution equation with the discrete force $G_i(\vec{r},t)$ is expressed as

$$f_i(\vec{r} + \vec{c}_i\delta t, t + \delta t) = f_i(\vec{r},t) - \frac{1}{\tau}\left[ f_i(\vec{r},t) - f_i^{\mathrm{eq}}(\vec{r},t) \right] + G_i(\vec{r},t)\delta t, \quad (6)$$

where $f_i(\vec{r},t)$ is the particle density distribution function at position $\vec{r}$ and time $t$ in the $i$th direction. $\tau$ is the single relaxation time related to the kinematic viscosity $\upsilon$, i.e., $\upsilon = c^2\delta t(2\tau - 1)/6$. $f_i^{\mathrm{eq}}(\vec{r},t)$ is the equilibrium distribution function and is determined by taking the expression of the Maxwell-Boltzmann distribution up to $O(v^2)$ [22],

$$f_i^{\mathrm{eq}} = \rho w_i \left[ 1 + \frac{3\vec{c}_i \cdot \vec{v}}{c^2} + \frac{9(\vec{c}_i \cdot \vec{v})^2}{2c^4} - \frac{3\vec{v} \cdot \vec{v}}{2c^2} \right], \quad (7)$$

where $\rho = \sum_i f_i$ is the local fluid density, $\vec{v} = \sum_i f_i \vec{c}_i/\rho + G\delta t/(2\rho)$ is the flow velocity, where $G$ is the forcing term, and $w_i$ is the weight coefficient determined by the discrete velocity model to ensure the mass and momentum conservation, i.e., $w_0 = 4/9$, $w_{1-4} = 1/9$, and $w_{5-8} = 1/36$ for the D2Q9-lattice velocity model. The discrete force is given by

$$G_i = \left(1 - \frac{1}{2\tau}\right) w_i \left[ 3\frac{\vec{c}_i - \vec{v}}{c^2} + \frac{9(\vec{c}_i \cdot \vec{v})\vec{c}_i}{2c^4} \right] \cdot G$$

$$\text{with} \quad G = G_D + G_B, \quad (8a)$$

$$G_D(\vec{r},t) = -\frac{2\rho\upsilon h\phi_3}{W_0^2}(1 - \phi_3)^2\vec{v}, \quad (8b)$$

$$G_B(\vec{r},t) = -\rho\vec{g}\beta_c(C - C_0)\phi_3, \quad (8c)$$

where $G_D$ is the dissipative drag force in the vicinity of the S/L interface to satisfy the no-slip boundary condition, which serves as a distributed momentum sink that forces the liquid velocity to vanish as the liquid fraction (i.e., $\phi_3$) approximates 0 [18]. $h = 2.757$ is a dimensionless constant obtained by an asymptotic analysis of plane flow past the diffusive interface [17]. $W_0$ is the interface thickness, and is fixed at $7\Delta x_{\min}$, which is a good compromise between the minimization of the grid anisotropy and the maximization of the computational efficiency by preliminary computations. $G_B$ is the buoyancy force induced by the concentration difference in the liquid [51]. $\vec{g} = 9.8\ \mathrm{m/s^2}$ is the gravitational acceleration vector along the negative $y$-axis direction, $\beta_c$ is the solute expansion coefficient, and $C_0$ is the initial liquid concentration. In addition, a bounce-back scheme [52] is employed at the moving S/L interface to ensure the conservation of the mass and momentum, i.e., $f_i(\vec{r},t,\vec{c}_i) = f_i(\vec{r},t,-\vec{c}_i)$.

### C. Numerical approach

The para-AMR algorithm with block structure adaptive mesh refinement and parallel computing scheme was employed to solve the phase-field lattice-Boltzmann equations. The detail of this algorithm was illustrated elsewhere [45,46] and only brief descriptions will be given here.

TABLE I. Thermophysical parameters of Al-Cu and $CBr_4$-$C_2Cl_6$ alloys.

| Parameters | Al-Cu | $CBr_4$-$C_2Cl_6$ |
|---|---|---|
| $D_L$ [solute diffusivity in liquid, ($m^2$/s)] | $3 \times 10^{-9}$ [51,57] | $5 \times 10^{-10}$ [33,58] |
| $D_S$ [solute diffusivity in solid ($m^2$/s)] | $3 \times 10^{-13}$ [51,57] | $5 \times 10^{-14}$ [33,58] |
| $m_\alpha$ [liquidus slope of $\alpha$ phase at eutectic temperature (K/mol frac)] | –1050 [59,60] | –81 [33,58] |
| $m_\beta$ [liquidus slope of $\beta$ phase at eutectic temperature (K/mol frac] | 488 [59,60] | 165 [33,58] |
| $k_\alpha$ (partition coefficient in $\alpha$ phase to the liquid phase) | 0.14 [51,57] | 0.75 [33,58] |
| $k_\beta$ (partition coefficient in $\beta$ phase to the liquid phase) | 1.85 [57] | 1.6 [33,58] |
| $T_E$ [eutectic temperature (K)] | 821 [59,60] | 357.6 [33,58] |
| $C_E$ [eutectic concentration (mol frac)] | 0.173 [59,60] | 0.118 [33,58] |
| $\sigma_{\alpha L}$ [$\alpha$/L interface energy ($J/m^2$)] | $160.01 \times 10^{-3}$ [59] | $6.6 \times 10^{-3}$ [33,58] |
| $\sigma_{\beta L}$ [$\beta$/L interface energy ($J/m^2$)] | $88.363 \times 10^{-3}$ [59] | $5.8 \times 10^{-3}$ [33,58] |
| $\sigma_{\alpha\beta}$ [$\alpha/\beta$ interface energy ($J/m^2$)] | $219.484 \times 10^{-3}$ [59] | $11.5 \times 10^{-3}$ [33,58] |
| $\beta_c$ (solute expansion coefficient) | –0.73 [61,62] | 0.5 [33,58] |

The refinement process was begun by tagging the potential grids according to a predefined gradient criterion,

$$\max_{1\leqslant i\leqslant 3}(|\nabla\phi_i|) + E_c|\nabla C| + E_v\left(\sqrt{|\nabla u|^2 + |\nabla v|^2}\right) \geqslant \xi, \quad (9)$$

where $E_c$ and $E_v$ are the weight coefficients for solute and velocity, respectively, and $\xi$ is a threshold value determined via numerical tests. $u$ and $v$ are the two axial velocity components, i.e., $\vec{v} = (u,v)$. The S/L interface during solidification is the position where the gradient reaches the local maximum and thus mesh refinement is needed. On each grid level, a cluster algorithm developed by Berger and Rigoutsos [53] was adopted to separate the tagged points into clusters or patch boxes. After constructing a hierarchical architecture with different sets of patch boxes on each grid level, the local data was then broadcast to all processors to realize the parallel computation.

To achieve effective communication between neighboring patch boxes, a layer of ghost cells was added at the external boundaries of each patch box to receive the data from its nearest neighbors. For interior boundaries, the restriction (i.e., updating values on the coarse grid using those from the fine grid) and interpolation (i.e., updating values on the fine grid using those from the coarse grid) processes were performed between different levels. Besides, to maintain the fluid viscosity as a constant in different levels, the relaxation time $\tau$ in Eq. (6) needed to vary with the grid size, i.e.,

$$\tau_f = 2(\tau_c - 1/2) + 1/2, \quad (10)$$

where $\tau_f$ and $\tau_c$ are the relaxation time at the fine and coarse grid level, respectively, and the spacing ratio of the coarse to fine grid is 2. In addition to the restriction on the relaxation time, the hydrodynamical variables and their derivatives should also be continuous over the coarse/fine interface [54,55]. Therefore, special attention was paid to the distribution function, which was rewritten as the sum of the equilibrium and nonequilibrium state.

$$f_{if}(\vec{r},t) = \alpha\tilde{f}_{ic}(\vec{r},t) + (1-\alpha)\tilde{f}_{ic}^{\rm eq}(\vec{r},t), \quad (11a)$$

$$f_{ic}(\vec{r},t) = \frac{1}{\alpha}f_{if}(\vec{r},t) + \left(1-\frac{1}{\alpha}\right)f_{if}^{\rm eq}(\vec{r},t), \quad (11b)$$

where $\alpha = 0.5\,\tau_f/\tau_c$ is a weight coefficient and the subscripts $f$ and $c$ denote the fine and coarse grid level, respectively. $\tilde{f}_{ic}$ denotes the spatially and temporally interpolated values from the coarse grid level.

### D. Materials

Two typical eutectic alloys including Al-Cu and $CBr_4$-$C_2Cl_6$ alloys were simulated in this work. The initial solute concentration $C_0$ was set as the eutectic point, i.e., 0.173 mole fraction (mol frac) for Al-Cu and 0.118 mol frac for $CBr_4$-$C_2Cl_6$, respectively, and related thermophysical parameters are provided in Table I. The minimum mesh size was 0.2 $\mu$m, and the number of the grid level was 3. The time step was dependent on the liquid solute diffusivity. Taking the Al-Cu alloy, for instance, the time step was $2.67 \times 10^{-6}$ s due to the stability limit of the explicit discretization scheme [45]. To investigate the effect of natural convection, as performed by Takaki *et al.* [51], we changed the magnitude of the solute expansion coefficient to predict the morphology evolution.

According to [56] [or see Eq. (A1) in the Appendix], the minimum-undercooling lamellar spacing was computed as 6.84 $\mu$m for Al-Cu and 9.81 $\mu$m for $CBr_4$-$C_2Cl_6$, respectively, which were actually the reference values in our simulations. Note that the two eutectic alloys have been widely investigated by *in situ* observations and systematic experiments, and the most remarkable difference is the interfacial width ratio of two coexisting solid phases. Based on the lever rule, the ratio of Al-Cu is 1:1, while that of $CBr_4$-$C_2Cl_6$ is approximately 2:1 because the weight of the $\beta$ phase is 0.29.

## III. RESULTS

The eutectic model under the nonconvection condition has been exhaustively studied by direct comparisons with experimental observations in our previous work [35]. To test the accuracy of the flow field, the lid-driven cavity flow was used as a test benchmark [21]. The top boundary moves from left to right with velocity $U = 0.1$, and related results are shown in Fig. 2. The velocity profiles changed from curved at a lower Reynolds (Re) number to linear at a higher Re number, and the nearly linear velocity profiles in the central core of the cavity indicated that the uniform vorticity region generated at a higher Re number, e.g., Re = 1000, 2000, and 5000, which agreed well with the classical test results [63–66]. Taking Re = 1000, for instance, as shown at the upper-right corners of

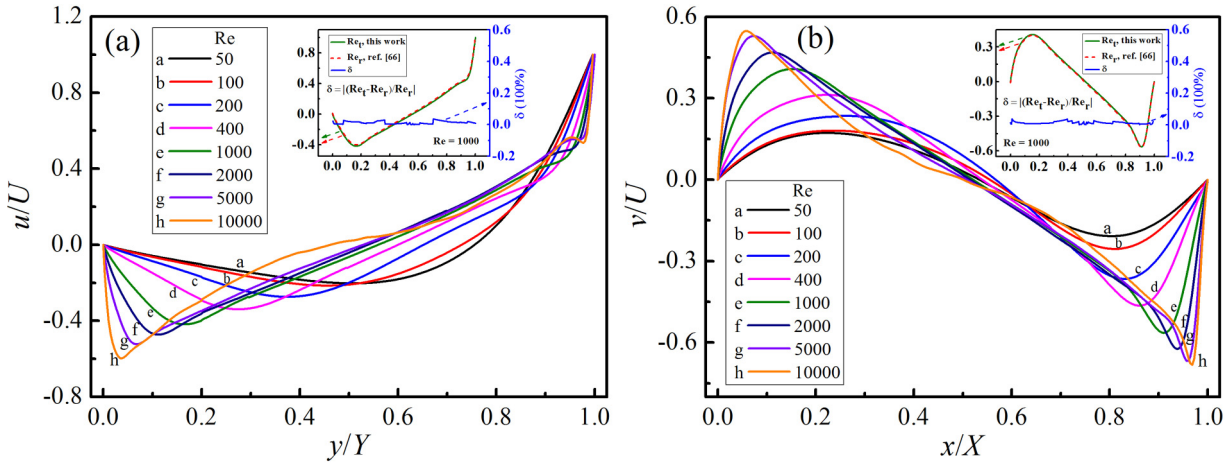


FIG. 2. Velocity components along the vertical ($y$) and horizontal ($x$) centerlines for the lid-driven cavity flow testing case. Different curves represent cases with different Reynolds (Re) numbers, including 50, 100, 200, 400, 1000, 2000, 5000, and 10 000. The inset at the upper-right corner of each figure shows the relative error between the current result and that from [66] for Re = 1000.

Fig. 2, it is clear that the simulated velocity values agreed quite well with those from [66]. The largest relative error between this work and [66] was about 2.31% for transverse velocity $u$ and 1.83% for longitudinal velocity $v$, respectively.

Figure 3 shows typical simulation results including the solute field and velocity field for Al-Cu and $CBr_4$-$C_2Cl_6$ alloys. The eutectic growth direction was along the positive $y$-axis direction, i.e., inverse to the gravitational direction. The solute expansion coefficient was set to be $-7.3 \times 10^{-4}$ and $5 \times 10^{-4}$, respectively, i.e., 1000 times lower than the real magnitude. Under that condition, the effect of convection on the eutectic morphology could be neglected, and we focused on the velocity direction and flow field. As shown in Figs. 3($a_1$) and 3($b_1$), the velocity direction in front of the growing interface is from the $\alpha$ to the $\beta$ phase for the Al-Cu alloy and from the $\beta$ to the $\alpha$ phase for the $CBr_4$-$C_2Cl_6$ alloy. The contour map of the velocity $\vec{v} = (u, v)$ is shown in Figs. 3($a_2$)–3($a_4$) and 3($b_2$)–3($b_4$), in which a darker color represents a larger value, and the red arrows point to the direction of the increasing velocity. For the Al-Cu alloy [see Fig. 3($a_2$)], the transverse velocity contour map was almost symmetric about the triple point due to the same interfacial width of the $\alpha$ and $\beta$ phase, while for the $CBr_4$-$C_2Cl_6$ alloy [see Fig. 3($b_2$)], the outlines of the transverse velocity contour map were offset to the center of the $\alpha$ phase due to the larger width of the $\alpha$ phase. For the longitudinal velocity, the contour map was symmetric about the centerline of the solid phases for both alloys. Although the two components of the velocity vector near the $\alpha$/L interface had opposite variation trends with those near the $\beta$/L interface, the magnitude of the total velocity presented a similar decreasing trend for both $\alpha$/L and $\beta$/L interfaces.

Figure 4 shows the distribution of the solute concentration along the given direction (i.e., $V_1$ and $V_2$) perpendicular to the S/L interface for the Al-Cu alloy. $C_{\alpha L}$ and $C_{\beta L}$ are the liquid concentration in equilibrium with the $\alpha$ and $\beta$ phase at temperature $T$, respectively, as schematically illustrated in the phase diagram at the upper-right corner. As the distance away from the S/L interface increased, the solute concentration changed monotonically until reaching a constant, i.e., 0.172 19 as indicated by the dotted line in Fig. 4. Such behavior could be best described by an exponential fitting function, i.e., $y = y_0 + A\exp(\omega x)$, and detailed parameters are given in Table II.

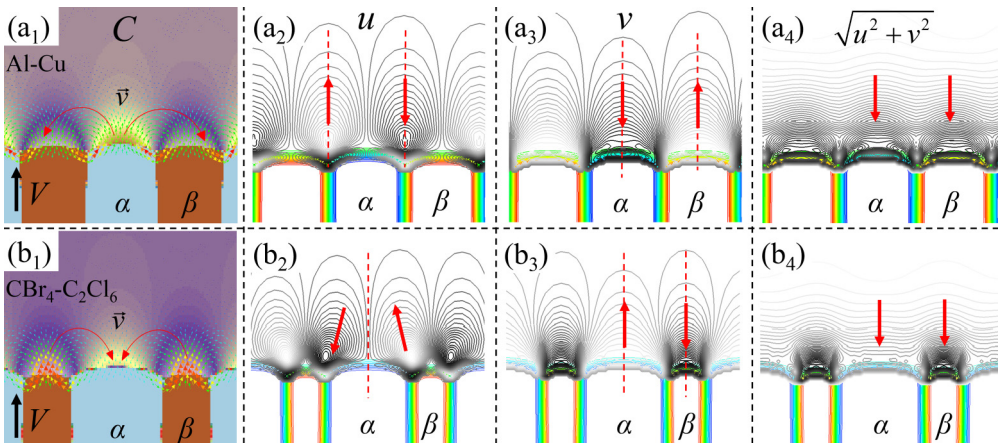


FIG. 3. Simulation results including the solute field and velocity field for Al-Cu ($a_1$)−($a_4$) and $CBr_4$-$C_2Cl_6$ alloys ($b_1$)−($b_4$). ($a_1$), ($b_1$) Solute field. ($a_2$)−($a_4$), ($b_2$)−($b_4$) The isolines of the transverse, longitudinal, and total velocity, respectively.

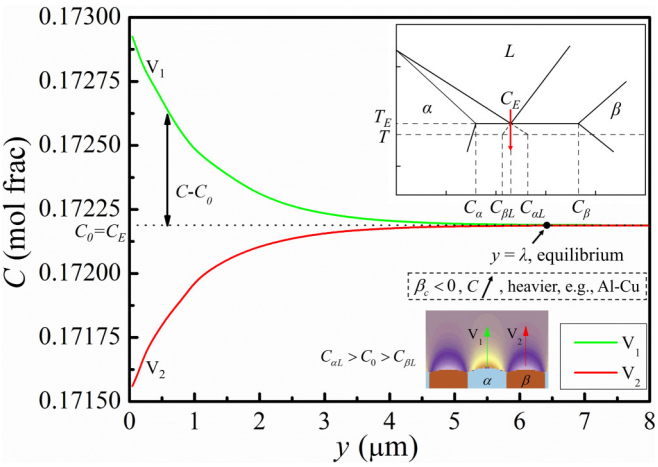


FIG. 4. Distribution of solute concentration along the direction perpendicular to the S/L interface for Al-Cu alloy.

The solute concentration reached its equilibrium value at about $y = \lambda$ ($\lambda$ is the lamellar spacing), indicating that the transition to the equilibrium state only took about one lamellar spacing.

The concentration difference, i.e., $C$-$C_0$, was converted to the mass difference by multiplying the solute expansion coefficient $\beta_c$ [see Eq. (8c)]. A negative $\beta_c$ indicates that the larger the concentration, the heavier the liquid phase [51]. For instance, for the Al-Cu alloy with negative $\beta_c$, a larger concentration means that the liquid has more Cu atoms and thus will be heavier. $C_{\alpha L}$ is larger than $C_{\beta L}$ and thus the liquid concentration near the $\alpha$/L interface is heavier for the Al-Cu alloy. Figure 5 shows the solute concentration distribution and mass difference near the S/L interface. As the distance away from the S/L interface increased, the concentration near the $\alpha$/L interface decreased while that near the $\beta$/L interface increased until approaching the far-field concentration (i.e., the initial concentration $C_0$). Accordingly, as the distance increased, the liquid near the $\alpha$/L interface will become increasingly lighter due to fewer Cu atoms, which is just the opposite for that near the $\beta$/L interface. It is noted that the solute concentration near the $\alpha$/L interface is always higher than that near the $\beta$/L interface and thus the liquid near the $\alpha$/L interface is heavier for the Al-Cu alloy. Because the buoyancy force induced by the mass difference will drive the liquid flow into the lighter region, there will be an outflow from the $\alpha$ phase and an inflow to the $\beta$ phase for the Al-Cu alloy, as shown in Figs. 3($a_1$) and 5. For the $CBr_4$-$C_2Cl_6$ alloy, the solute expansion coefficient is positive and thus the liquid phase with larger concentration will be lighter. The corresponding velocity vector will point to the $\alpha$ phase from the $\beta$ phase, which is just the opposite as shown in Figs. 3($b_1$) and 5.

Figures 6(a) and 6(b) show the distribution of the velocity and solute concentration along the direction parallel to the S/L interface at $y = 0.05S_{\alpha\beta}$($S_{\alpha\beta} = \lambda/2$) away from the interface for the Al-Cu and $CBr_4$-$C_2Cl_6$ alloys, respectively, and the minus velocity indicates that the velocity is along the negative axis direction. The concentration-distance curves exhibited a sinusoidal variation, i.e., $y = y_0 + A\sin[\pi(x-x_c)/\omega]$, which agreed with that derived by Jackson and Hunt [1], and detailed parameters are given in Table II. The average solute concentration was denoted by the horizontal dotted red line, which deviated from the zero-velocity line (i.e., the horizontal dotted black line). This is because the position of the average concentration was not strictly on the triple point [7], though the longitudinal velocity became zero at this position [see the green circles in Figs. 6(a) and 6(b)]. Taking the $CBr_4$-$C_2Cl_6$ alloy, for instance, the volume fraction of the minor phase (i.e., $\beta$ phase) is approximately 0.29, and thus the position of the average concentration was not on the triple point but significantly shifted towards the centerline of the $\alpha$ phase [see the red triangles in Fig. 6(b)] [35]. When the width ratio of the two solid phases is almost equal, e.g., the Al-Cu alloy, the position of zero longitudinal velocity would overlap with that of average concentration. Furthermore, if the velocity sign was not considered, the velocity-$x$ curves including transverse velocity, longitudinal velocity, and total velocity all presented symmetric patterns about the centerline of the solid phase, which agreed well with the velocity contour map in Figs. 3($a_2$)–3($a_4$) and 3($b_2$)–3($b_4$). Meanwhile, as discussed before, the sign of the velocity including the transverse velocity and longitudinal velocity was precisely the opposite in the Al-Cu alloy compared to the $CBr_4$-$C_2Cl_6$ alloy due to the sign difference of the solute expansion coefficient. For the total velocity, the values at the midpoint of the $\alpha$/L and $\beta$/L interfaces were almost equal for the Al-Cu alloy, while those for the $CBr_4$-$C_2Cl_6$ alloy were significantly different.

Figures 6(c) and 6(d) show a more quantitative description of the two velocity components for the $CBr_4$-$C_2Cl_6$ alloy. In the half lamellar spacing, i.e., from the centerline of the $\alpha$ phase to that of the $\beta$ phase, the transverse velocity underwent a maximum and then decreased as $x$ increased. The maximum occurred at the three-phase junction when $y = 0.12S_{\alpha\beta}$ and was 0.26 $\mu$m/s, which was approximately one half of the maximum longitudinal velocity in Fig. 6(d). When $y = 0.5S_{\alpha\beta}$, the local maximum reduced to 0.1 $\mu$m/s and then decreased rapidly as $y$ increased. Away from the interface, the position corresponding to the maximum of the transverse velocity first

TABLE II. Parameters of the fitting functions for the solute concentration near the interface.

| Alloy | Source | Fitting function | $y_0$ | $A$ | $\omega$ | $x_c$ | Reduced chi square[a] | Adj. $R$ square[b] |
|---|---|---|---|---|---|---|---|---|
| Al-Cu | Fig. 4: $V_1$ | $y = y_0 + A\exp(\omega x)$ | 0.17219 | $7.6414\times10^{-4}$ | −0.92389 | | $1.4139\times10^{-11}$ | 0.99975 |
| | Fig. 4: $V_2$ | | 0.17219 | $-6.5533\times10^{-4}$ | −1.0600 | | $2.1438\times10^{-11}$ | 0.99945 |
| | Fig. 6(a) | $y = y_0 + A\sin[\pi(x-x_c)/\omega]$ | 0.17219 | $7.3630\times10^{-4}$ | 3.3557 | 4.8784 | $2.5740\times10^{-10}$ | 0.99909 |
| $CBr_4$-$C_2Cl_6$ | Fig. 6(b) | | 0.11825 | $2.0282\times10^{-4}$ | 5.9242 | −2.3017 | $1.9003\times10^{-11}$ | 0.99916 |

[a]Reduced chi square: equivalent to residual mean square in the analysis of variance and the smaller the value, i.e., closer to zero, the higher the fitting degree [67].

[b]Adj. $R$ square: an adjusted version of $R$ square, which satisfies that the closer to 1, the more accurate the fitting function [67].

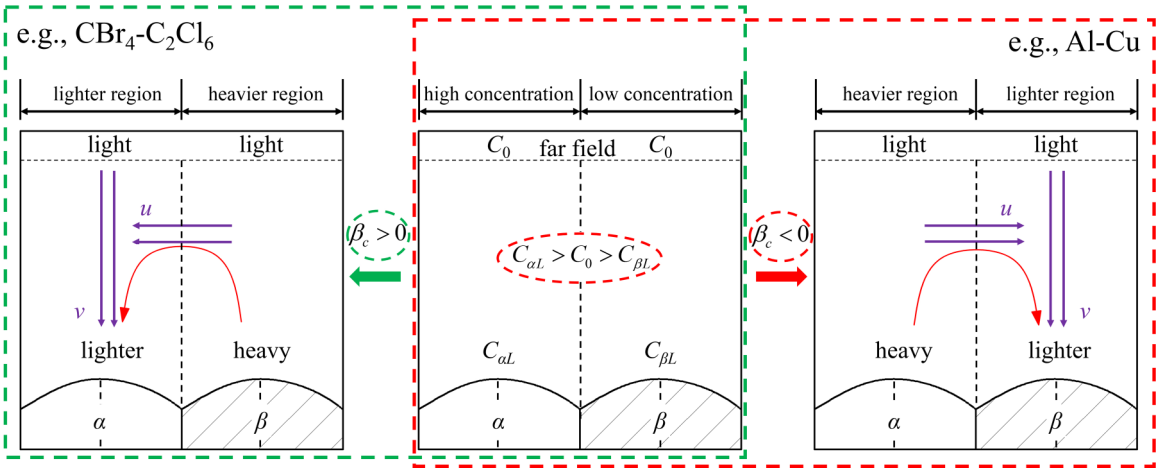


FIG. 5. Schematic illustration of solute concentration distribution and mass difference near S/L interface.

moved to the three-phase junction and then the middle of the $\alpha$ phase, as marked by the black arrows in Fig. 6(c). The inset at the bottom-left corner of Fig. 6(c) shows the velocity distribution in a lamellar spacing at the distance $y = 0.5S_{\alpha\beta}$. Similar to that in Fig. 6(b), the absolute value of the transverse velocity was symmetric about the centerline of the solid phase, though the shape of the $u$-$x$ curve was different.

For the longitudinal velocities in Fig. 6(d), after experiencing a maximum, the velocities along the given directions (i.e., $V_1$, $V_2$, $V_3$, $V_4$) started to decrease and then intersected at $y = 1.25S_{\alpha\beta}$, after which the longitudinal velocity remained at a relatively low value. The position of its maximum was closer to the S/L interface with decreasing distance away from the centerline of the $\beta$ phase, as marked by the black arrow in Fig. 6(d).

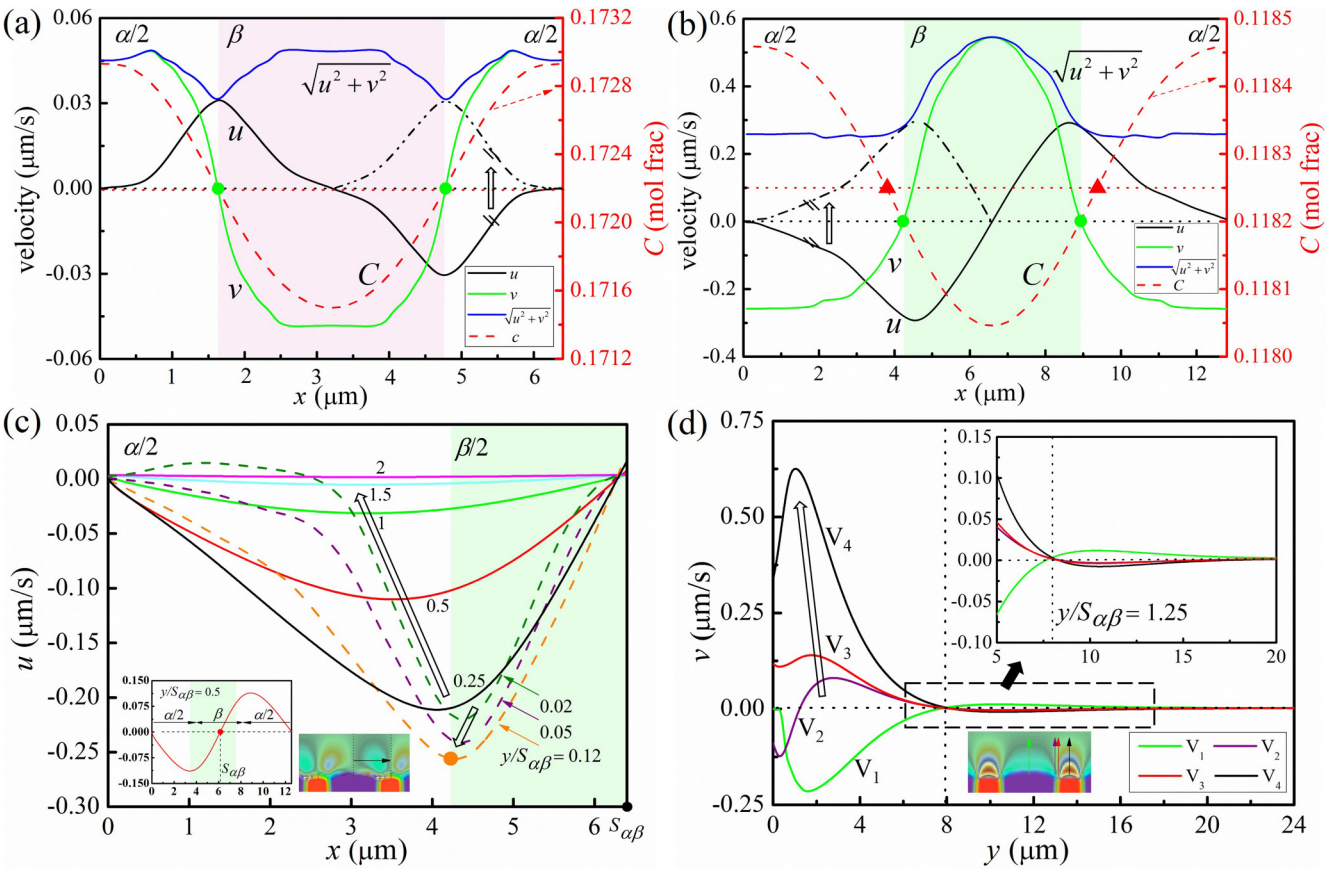


FIG. 6. (a),(b) show the distribution of velocity and solute concentration along the direction parallel to the S/L interface at $y = 0.05S_{\alpha\beta}(S_{\alpha\beta} = \lambda/2)$ away from the interface for Al-Cu and $CBr_4$-$C_2Cl_6$ alloys, respectively. (c),(d) show a more quantitative description of two velocity components for the $CBr_4$-$C_2Cl_6$ alloy. (c) shows the distribution of the transverse velocity along the direction parallel to the S/L interface at different distances away from the interface. (d) shows the distribution of the longitudinal velocity along the direction perpendicular to the S/L interface.

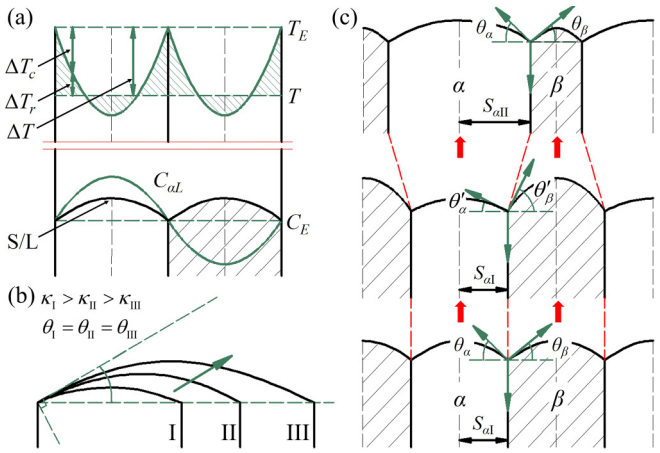


FIG. 7. Schematic illustrations of the interfacial temperature compensation, curvature adjustment, and width adjustment, respectively.

## IV. DISCUSSION

### A. Growth undercooling

The stability of the S/L interface is largely dependent on the local undercooling, i.e., the difference between the eutectic temperature $T_E$ and the actual temperature $T$. During solidification, the kinetic undercooling could be normally ignored because for most regular eutectic systems, the kinetic undercooling is much smaller than either the constitutional undercooling or the curvature undercooling [1,68]. Therefore, as shown in Fig. 7(a), the temperature difference $\Delta T$ can be expressed as

$$\Delta T = T_E - T = \Delta T_c + \Delta T_r, \tag{12}$$

where the constitutional undercooling, i.e., $\Delta T_c = m[C_E - C_{y=0}(x)]$, denotes the departure of the local interfacial composition $C_{y=0}(x)$ from the eutectic composition $C_E$, where $m$ is the liquidus slope. The curvature undercooling, i.e., $\Delta T_r = \Gamma\kappa(x)$, represents the effect of the interfacial curvature on the equilibrium temperature, where $\Gamma$ is the Gibbs-Thomson coefficient, and $\kappa(x)$ is the local interfacial curvature.

Assuming that the real interface shape is described by the relation $y = I(x)$, the average curvature of the $\alpha$/L interface is given by

$$\begin{aligned}\langle\kappa_\alpha(x)\rangle &= \frac{1}{2S_\alpha}\int_{-S_\alpha}^{S_\alpha}\kappa_\alpha(x)dx \\ &= \frac{1}{2S_\alpha}\int_{-S_\alpha}^{S_\alpha}\frac{-d^2I/dx^2}{[1+(dI/dx)^2]^{3/2}}dx \\ &= -\frac{1}{2S_\alpha}\sin\tan^{-1}\left(\frac{dI}{dx}\right)\Big|_{-S_\alpha}^{S_\alpha} = \frac{\sin\theta_\alpha}{S_\alpha},\end{aligned} \tag{13}$$

where $\langle\cdot\rangle$ denotes the average operation, $S_\alpha$ is the half width of the $\alpha$ phase. and $\theta_\alpha$ is the contact angle at the $\alpha$/L interface as shown in Figs. 1 and 7(c). At the triple junction, the local equilibrium requires that the surface tensions should satisfy

$$\sigma_{\alpha L}\sin\theta_\alpha + \sigma_{\beta L}\sin\theta_\beta = \sigma_{\alpha\beta}, \tag{14a}$$

$$\sigma_{\alpha L}\cos\theta_\alpha = \sigma_{\beta L}\cos\theta_\beta, \tag{14b}$$

where $\sigma_{\alpha L}$, $\sigma_{\beta L}$, and $\sigma_{\alpha\beta}$ are the surface tensions at the $\alpha$/L, $\beta$/L, and $\alpha/\beta$ interfaces, respectively, and $\theta_\beta$ is the contact angle at the $\beta$/L interface. Note that $\theta_\alpha$ and $\theta_\beta$ are uniquely determined by the force balance at the triple junction, and are constant if the surface tension anisotropy is neglected. Accordingly, $\Delta T_r$ will be altered by adjusting $S_\alpha$ and $S_\beta$ from Eq. (13).

The presence of the natural convection will change the concentration field and thus the interfacial constitutional undercooling. Figure 8(a) shows the solute concentration of the Al-Cu alloy at the specific point (i.e., $\phi_1 = \phi_3 = 0.5$) of the $\alpha$/L interface varying with the solute expansion coefficient $\beta_c$. To investigate the effect of the natural convection, $\beta_c$ varied from $10^{-4}\beta_{c0}$ to $10^{1}\beta_{c0}$ in units of $|\beta_{c0}| = 7.3\times10^{-1}$. The increase of $|\beta_c|$ (i.e., the convection intensity) could significantly alter the concentration near the $\alpha$/L interface in contrast with that under the nonconvection condition. Accordingly, $\Delta T_c$ was changed to accommodate this variation.

However, the temperature field is imposed by the macroscopic heat fluxes, i.e., assumed to be isothermal with constant undercooling $\Delta T$ in this work. To adapt to the changing

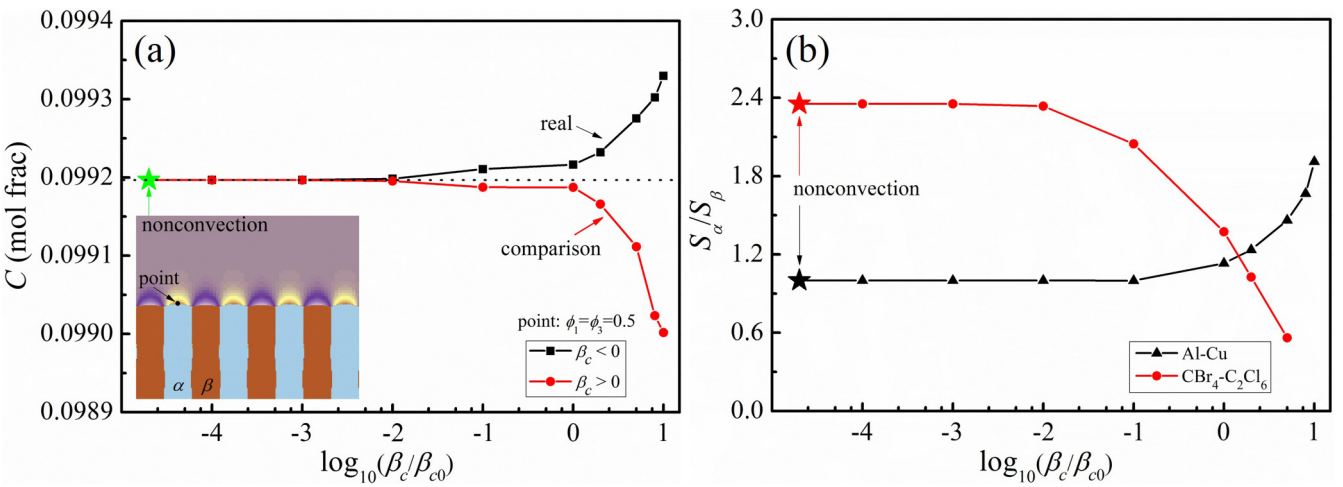


FIG. 8. (a) Solute concentration of the Al-Cu alloy at the specific point of the $\alpha$/L interface (i.e., $\phi_1 = \phi_3 = 0.5$) versus solute expansion coefficient. (b) Simulated width ratio versus solute expansion coefficient for Al-Cu and $CBr_4$-$C_2Cl_6$ alloys.

TABLE III. Parameters of the exponential fitting functions for the width ratio varying with the solute expansion coefficient.

| Alloy | Fitting function | $\zeta_0$ | $A$ | $\tau$ | Reduced chi square[a] | Adj. $R$ square[b] |
|---|---|---|---|---|---|---|
| Al-Cu | $\zeta = \zeta_0 + A\exp[\frac{1}{\tau}\log_{10}(\frac{\beta_c}{\beta_{c0}})]$ | 1.0005 | 0.1139 | 0.4911 | $8.165 \times 10^{-4}$ | 0.9929 |
| $CBr_4$-$C_2Cl_6$ | | 2.4399 | −1.0391 | 1.1376 | $4.190 \times 10^{-3}$ | 0.9922 |

[a]Reduced chi square: equivalent to residual mean square in the analysis of variance and the smaller the value, i.e., closer to zero, the higher the fitting degree [67].

[b]Adj. $R$ square: an adjusted version of $R$ square, which satisfies that the closer to 1, the more accurate the fitting function [67].

difference between $\Delta T$ and $\Delta T_c$, $\Delta T_r$ needs to be adjusted by changing the shape of the S/L interface. Figures 7(b) and 7(c) show the schematic illustrations of the adjustment of the curvature and the lamellar width, respectively. Taking the $\alpha$/L interface of the Al-Cu alloy, for instance, when the solute expansion coefficient was negative [i.e., the real value $\beta_c < 0$ in Fig. 8(a)], the flow direction was from the $\alpha$ to the $\beta$ phase [see Fig. 3($a_1$)]. Accordingly, large numbers of solute atoms near $\alpha$/L interface were transported into the liquid in a timely manner, which contributed to the solute precipitation of the $\alpha$ phase. As a result, the interfacial solute concentration became larger [see Fig. 8(a)], as well as the concentration difference $C$-$C_0$ and $\Delta T_c$. To maintain an isothermal $\alpha$/L interface, $\Delta T_r$ needs to be decreased via adjusting the local interfacial curvature. According to Eq. (13), such adjustment was accomplished by increasing the half width of the $\alpha$ phase in terms of average effects, i.e., from type I to type II or III ($\kappa_{\rm I} > \kappa_{\rm II} > \kappa_{\rm III}$) while maintaining the contact angles unchanged ($\theta_{\rm I} = \theta_{\rm II} = \theta_{\rm III}$) [see Fig. 7(b)]. This adjustment could actually attribute to the movement of the triple point, as shown in Fig. 7(c). Taking the Al-Cu alloy, for instance, when the convection increased $\Delta T_c$ of the $\alpha$/L interface but reduced $\Delta T_c$ of the $\beta$/L interface, $\Delta T_r$ needed to have the opposite adjustment to compensate for the variation. It is noted that $\Delta T_r$ is given in average by $\Gamma_i \sin\theta_i / S_i (i = \alpha, \beta)$, which led to a lower $\theta_\alpha$ but larger $\theta_\beta$. To restore the contact angles back to the equilibrium values, the two-phase width $S_i$ was adjusted to regulate the interfacial concentration distribution by the movement of the triple point. Once the correct contact angles were established, the two-phase width reached steady state, and then the eutectic lamellae solidified in a globally equivalent mode with that of single phase [68].

To clearly illustrate the lamellar adjustment, the width ratio $\zeta = S_\alpha / S_\beta$ was introduced, and Fig. 8(b) shows the width ratio $\zeta$ varying with the solute expansion coefficient $\beta_c$ in units of $\beta_{c0} = -7.3 \times 10^{-1}$ and $5.0 \times 10^{-1}$ for the Al-Cu and $CBr_4$-$C_2Cl_6$ alloys, respectively. As $|\beta_c|$ increased, $\zeta$ increased for the Al-Cu alloy, while it decreased for the $CBr_4$-$C_2Cl_6$ alloy. To reveal the mechanism of the lamellar adjustment, the nonlinear variation of $\zeta$ versus $\beta_c$ was fitted by an exponential function, i.e., $\zeta = \zeta_0 + A\exp[\frac{1}{\tau}\log_{10}(\frac{\beta_c}{\beta_{c0}})]$, where $\beta_c/\beta_{c0}$ denotes the magnification of the convection intensity; related fitting parameters are detailed in Table III. The relaxation factor $\tau$ in the fitting function is used to predict the extent to which the change of solute expansion coefficient $\beta_c$ affects the lamellar width ratio. For the Al-Cu alloy, the factor $\tau$ is 0.4911 and smaller than that of the $CBr_4$-$C_2Cl_6$ alloy (i.e., 1.1376), indicating that the Al-Cu alloy is more sensitive to the change of the convection intensity. The amplitude $A$ denotes the variation amount under the same magnification of the convection intensity. The amplitude of the $CBr_4$-$C_2Cl_6$ alloy is about one order of magnitude larger than that of the Al-Cu alloy, indicating that the width adjustment of the $CBr_4$-$C_2Cl_6$ alloy is more significant. As shown in Fig. 9, the corresponding nephogram of the solute field presented a different lamellar width ratio under different convection intensity, the magnitude of which, i.e., the magnification of $\beta_c$, is marked at the upper-right corner of each subfigure.

The presence of natural convection changed the interfacial concentration distribution, and then adjusted the lamellar width

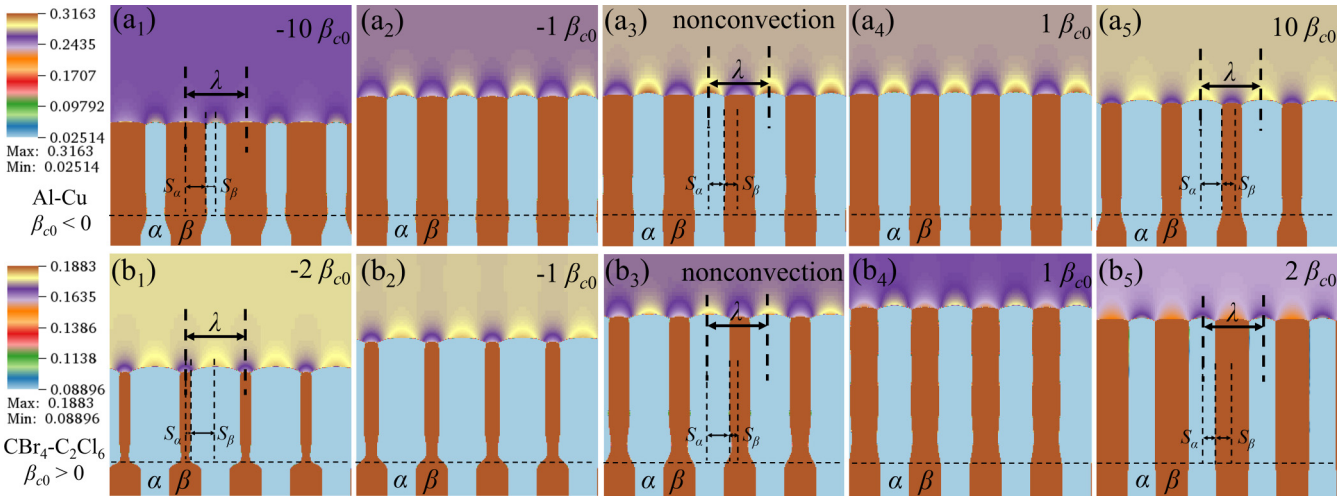


FIG. 9. Distribution of the solute field under different convection intensities for Al-Cu ($a_1$)−($a_5$) and $CBr_4$-$C_2Cl_6$ ($b_1$)−($b_5$) alloys. The convection intensity, i.e., the magnification of solute expansion coefficient, is marked at the upper-right corner of each subfigure.

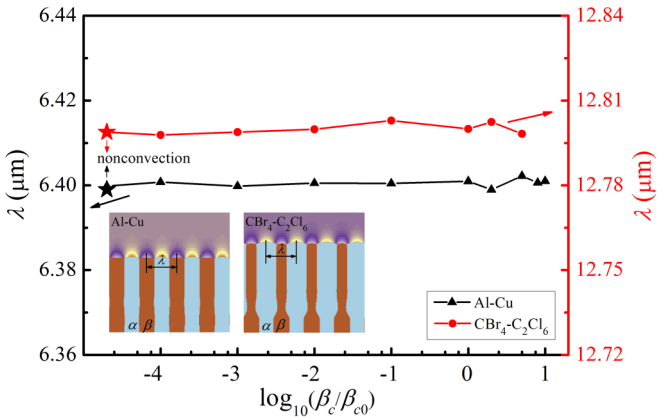


FIG. 10. Eutectic lamellar spacing versus solute expansion coefficient for Al-Cu and $CBr_4$-$C_2Cl_6$ alloys.

ratio to maintain local thermodynamic equilibrium. Note that if the solute expansion coefficient was too large, e.g., magnified by 100 times for the Al-Cu alloy or 10 times for the $CBr_4$-$C_2Cl_6$ alloy, the nearly planar S/L interface would become unstable, and the lighter phase (e.g., the $\alpha$ phase for the Al-Cu alloy) would protrude significantly into the liquid due to the enhanced fluid flow.

It is noted that with increasing convection intensity, the width of the two solid phases changed in the opposite direction, e.g., increasing for the $\alpha$ phase but decreasing for the $\beta$ phase for the Al-Cu alloy, while the lamellar spacing $\lambda$, i.e., 2 ($S_\alpha + S_\beta$), almost remained constant during all simulations, as shown in Fig. 10. The effect of the natural convection on the eutectic lamellar spacing was quite small in the eutectic alloy, which agreed well with the experimental results of Lee *et al.* [5].

### B. Thermodynamic equilibrium

Based on the steady-state eutectic growth theory established by Jackson and Hunt [1], the growth undercooling without convection could be deduced as a function of the growth velocity $V$ and the lamellar spacing $\lambda$.

$$\Delta T = K_1 \lambda V + K_2/\lambda, \tag{15a}$$

where $K_1$ and $K_2$ are given by

$$K_1 = \frac{\hat{m} C_0^* (1+\zeta)^2 P}{D\zeta}, \tag{15b}$$

$$K_2 = 2\hat{m}(1+\zeta)\left(\frac{\Gamma_\alpha \sin\theta_\alpha}{|m_\alpha|\zeta} + \frac{\Gamma_\beta \sin\theta_\beta}{m_\beta}\right), \tag{15c}$$

where $\hat{m} = |m_\alpha| m_\beta / (|m_\alpha| + m_\beta)$ is the harmonic average of the liquidus slopes $|m_\alpha|$ and $m_\beta$. $C_0^*$ is the solubility limit difference of two solid phases at the eutectic temperature. $P = \sum_{n=1}^{\infty} (\frac{1}{n\pi})^3 \sin^2(\frac{n\pi\zeta}{1+\zeta})$ is a function of the width ratio $\zeta$.

When the natural convection was considered in the microstructure evolution, the two-phase width needed to be adjusted to maintain the thermodynamic equilibrium. From Eqs. (15a)–(15c), this equilibrium, i.e., the competition between $\Delta T_c$ and $\Delta T_r$, did not result in a fixed relation between $V$ and $\lambda$ due to the change of $\zeta$. To further investigate the

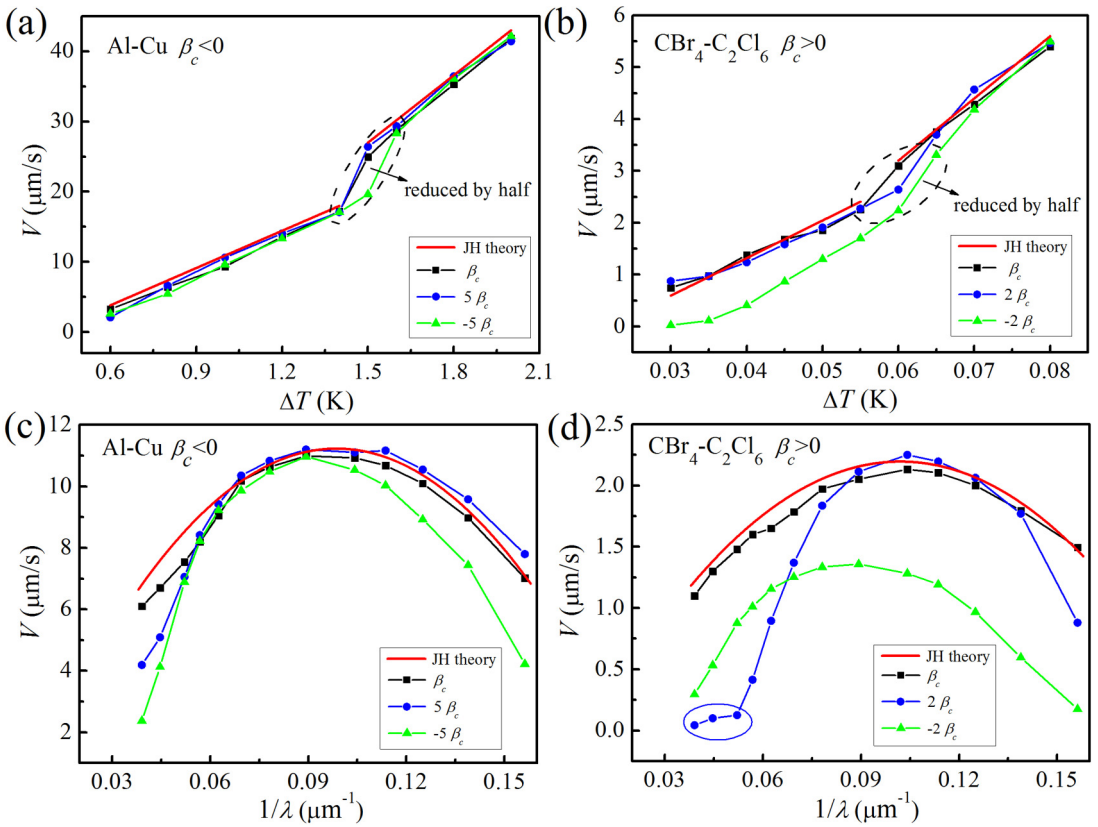


FIG. 11. Simulated growth velocity versus undercooling for (a) Al-Cu and (b) $CBr_4$-$C_2Cl_6$ alloys. Simulated growth velocity versus the inverse of the lamellar spacing for (c) Al-Cu and (d) $CBr_4$-$C_2Cl_6$ alloys.

TABLE IV. Parameters of the quadratic fitting functions for the growth velocity versus the inverse of the lamellar spacing.

| Alloy | Source | Fitting function | $a$ | $b$ | $c$ | Reduced chi square[a] | Adj. $R$ square[b] |
|---|---|---|---|---|---|---|---|
| Al-Cu | Fig. 11(c): $\beta_{c0}$ | $y = ax^2 + bx + c$ | –1247.5 | 249.06 | –1.3767 | 0.01248 | 0.95076 |
| | Fig. 11(c): $5\beta_{c0}$ | | –1644.2 | 343.70 | –3.3008 | 0.18703 | 0.94781 |
| | Fig. 11(c): $-5\beta_{c0}$ | | –2235.9 | 438.27 | –5.3051 | 0.04911 | 0.93715 |
| $CBr_4$-$C_2Cl_6$ | Fig. 11(d): $\beta_{c0}$ | | –243.06 | 51.475 | –0.5398 | 0.00108 | 0.99138 |
| | Fig. 11(d): $2\beta_{c0}$ | | –547.33 | 118.04 | –2.1504 | 0.06001 | 0.92099 |
| | Fig. 11(d): $-2\beta_{c0}$ | | –328.24 | 61.079 | –1.4704 | 0.00701 | 0.95679 |

[a]Reduced chi square: equivalent to residual mean square in the analysis of variance and the smaller the value, i.e., closer to zero, the higher the fitting degree [67].

[b]Adj. $R$ square: an adjusted version of $R$ square, which satisfies that the closer to 1, the more accurate the fitting function [67].

effect of the natural convection, a constant $\eta$ was introduced to reflect the width adjustment. The lamellar growth was simply assumed to occur at $\lambda = \eta\lambda_{nf}$, where $\lambda_{nf}$ is the lamellar spacing under the nonconvection condition. When $\eta = 1$, it was restored to the classical Jackson-Hunt (JH) theory [1]. In this respect, the eutectic growth could be described as

$$V = -\frac{K_2}{K_1\eta^2}\frac{1}{\lambda_{nf}^2} + \frac{\Delta T}{K_1\eta}\frac{1}{\lambda_{nf}}. \tag{16}$$

Figures 11(a) and 11(b) show the growth velocity $V$ as a function of the undercooling for two eutectic alloys. As the undercooling increased, the lamellar spacing was reduced by half, but the growth velocity continued to increase. Taking the Al-Cu alloy, for instance, for two cases including $\beta_{c0}$ and $5\beta_{c0}$, both lamellar spacings were reduced by half when the undercooling reached 1.5 K, while for the case $-5\beta_{c0}$, the turning point was 1.6 K. When the lamellar spacing remained unchanged, the growth velocity increased nearly linearly with the undercooling, as indicated by Eq. (16). The relation determined by the classical Jackson-Hunt theory is plotted in solid red lines. The presence of natural convection only affected the specific velocity magnitude, but kept the variation trend unchanged. Note that when the solute expansion coefficient of the $CBr_4$-$C_2Cl_6$ alloy was magnified by $-2$ times, the two-phase width difference became remarkable [see Fig. 9($b_1$)], and the growth velocity significantly slowed down due to increasing difficulty of solute diffusion.

Figures 11(c) and 11(d) show the growth velocity versus the inverse of the lamellar spacing for two eutectic alloys. Such variation could be best described by a quadratic fitting function, i.e., $y = ax^2 + bx + c$; detailed parameters are provided in Table IV, in which the parameter $c$ is close to 0. As specified in Eq. (16), when $K_1$, $K_2$, $\eta$, and $\Delta T$ are determined under the given convection condition, the velocity $V$ changes with $1/\lambda$ in a quadric relationship. However, in our limited simulations, when the initial lamellar spacing became too large (e.g., $\lambda \geqslant 19.2\ \mu$m or $1/\lambda \leqslant 0.052\ \mu\text{m}^{-1}$ for the $CBr_4$-$C_2Cl_6$ alloy), the eutectic couples would grow extremely slowly, as designated by the blue circle in Fig. 11(d). Furthermore, from the intercept (i.e., $-\frac{K_2}{K_1\eta^2}\frac{1}{\lambda_{nf}^2}$) and slope (i.e., $\frac{1}{K_1\eta\lambda_{nf}}$) of the linear functions [see Figs. 11(a) and 11(b)] and the position corresponding to the peak of the quadric functions [see Figs. 11(c) and 11(d)], the constant $\eta$ was smaller than 1, and the greater the convection intensity, the smaller the constant.

## V. CONCLUSIONS

The lamellar eutectic growth under natural convection for Al-Cu and $CBr_4$-$C_2Cl_6$ alloys was investigated by performing phase-field lattice-Boltzmann simulations. A para-AMR algorithm was employed to shorten the computation time. The simulation results were discussed and compared with theoretical predictions, based on which the following conclusions could be drawn:

(1) During the eutectic growth under natural convection, the transverse and longitudinal velocity near the S/L interface had different variation trends, but both presented symmetric patterns about the centerline of the solid phases. There is an outflow from the lighter phase and an inflow to the heavier phase, e.g., from the Al-rich phase to the Cu-rich phase for the Al-Cu eutectic alloy. The width ratio of two coexisting solid phases has significant influence on the distribution of the velocity field.

(2) The increase of the convection intensity would lead to the adjustment of both solute distribution and interfacial curvature, while the lamellar spacing remained constant. The effect of the natural convection on the width ratio $\zeta$ could be described by $\zeta = \zeta_0 + A\exp[\frac{1}{\tau}\log_{10}(\frac{\beta_c}{\beta_{c0}})]$, where $\beta_c/\beta_{c0}$ denotes the magnification of the convection intensity, $\tau$ reflects the level of difficulty of the adjustment, and $A$ denotes the variation amount to the change of convection intensity.

(3) The existence of natural convection changed the growth velocity, but had no influence on the steady-state eutectic growth rule proposed by Jackson and Hunt. By introducing a constant $\eta$ smaller than 1 into the growth rule, i.e., $V = -\frac{K_2}{K_1\eta^2}\frac{1}{\lambda_{nf}^2} + \frac{\Delta T}{K_1\eta}\frac{1}{\lambda_{nf}}$, where $\lambda_{nf}$ is the spacing under the nonconvection condition, the eutectic growth under natural convection could be revealed.

## ACKNOWLEDGMENTS

This work was supported by the Joint Funds of the National Natural Science Foundation of China (Grant No. U1537202), the Tsinghua-General Motors International collaboration project (Grant No. 20153000354), the UK Royal Society through the Newton International Fellowship Scheme, and the Tsinghua University Qingfeng Prepaid Scholarship. The authors would also like to thank the National Laboratory for Information Science and Technology in Tsinghua University for access to supercomputing facilities.

## APPENDIX: COMPUTATION OF THE MINIMUM-UNDERCOOLING LAMELLAR SPACING

According to Ref. [56], the minimum-undercooling lamellar spacing $\lambda_m$ could be determined by

$$\lambda_m = \sqrt{\frac{2D_l}{VC_0^* P(\zeta)}\left[\frac{\Gamma_\alpha \sin\theta_\alpha \zeta}{m_\alpha} + \frac{\Gamma_\beta \sin\theta_\beta (1-\zeta)}{m_\beta}\right]}, \quad \text{(A1)}$$

where $D_l$ is the liquid diffusion coefficient and $V$ is the growth velocity. $C_0^* = C_\beta - C_\alpha$ is the solubility limit difference of two solid phases (i.e., $\alpha$ and $\beta$ phases) at the eutectic temperature. $P(\zeta) = \sum_{n=1}^{\infty} (\frac{1}{n\pi})^3 \sin^2(\frac{n\pi\zeta}{1+\zeta})$ is a constant only dependent on the width ratio $\zeta$. $\Gamma_\alpha$ and $\Gamma_\beta$ are the Gibbs-Thomson coefficients of two solid phases. $\theta_\alpha$ and $\theta_\beta$ are the contact angles at the $\alpha$/L and $\beta$/L interface, respectively. $m_\alpha$ and $m_\beta$ are the liquidus slopes.


[1] K. A. Jackson and J. D. Hunt, Trans. Metall. Soc. AIME **236**, 1129 (1966).
[2] J. M. Quenisset and R. Naslain, J. Cryst. Growth **54**, 465 (1981).
[3] V. Baskaran and W. R. Wilcox, J. Cryst. Growth **67**, 343 (1984).
[4] D. Ma, W. Q. Jie, Y. Li, and S. C. Ng, Acta Mater. **46**, 3203 (1998).
[5] J. H. Lee, S. Liu, and R. Trivedi, Metall. Mater. Trans. A **36**, 3111 (2005).
[6] A. Zhang, Z. Guo, and S. Xiong, China Foundry **14**, 373 (2017).
[7] J. A. Dantzig and M. Rappaz, *Solidification* (EPFL Press, Lausanne, 2009).
[8] J. Du and B. Wen, Appl. Mater. Today **7**, 13 (2017).
[9] A. Zhang, S. Liang, Z. Guo, and S. Xiong, Exp. Therm. Fluid Sci. **88**, 472 (2017).
[10] S. R. Coriell, G. B. McFadden, W. F. Mitchell, B. T. Murray, J. B. Andrews, and Y. Arikawa, J. Cryst. Growth **224**, 145 (2001).
[11] W. M. Wang, Z. G. Liu, J. M. Liu, and X. Y. Chen, J. Cryst. Growth **240**, 313 (2002).
[12] R. Siquieri and H. Emmerich, Philos. Mag. **91**, 45 (2011).
[13] D. I. Popov, L. L. Regel, and W. R. Wilcox, Cryst. Growth Des. **1**, 313 (2001).
[14] S. Akamatsu and M. Plapp, Curr. Opin. Solid State Mater. Sci. **20**, 46 (2016).
[15] F. Drolet, K. R. Elder, M. Grant, and J. M. Kosterlitz, Phys. Rev. E **61**, 6705 (2000).
[16] D. Sun, M. Zhu, S. Pan, and D. Raabe, Acta Mater. **57**, 1755 (2009).
[17] C. Beckermann, H. J. Diepers, I. Steinbach, A. Karma, and X. Tong, J. Comput. Phys. **154**, 468 (1999).
[18] X. Tong, C. Beckermann, A. Karma, and Q. Li, Phys. Rev. E **63**, 061601 (2001).
[19] Z. Guo, J. Mi, S. Xiong, and P. S. Grant, Metall. Mater. Trans. B **44**, 924 (2013).
[20] Z. Guo, J. Mi, S. Xiong, and P. S. Grant, J. Comput. Phys. **257**, 278 (2014).
[21] A. A. Mohamad, *Lattice Boltzmann Method* (Springer, London, 2011).
[22] S. Chen and G. D. Doolen, Annu. Rev. Fluid. Mech. **30**, 329 (1998).
[23] W. Miller, S. Succi, and D. Mansutti, Phys. Rev. Lett. **86**, 3578 (2001).
[24] D. Medvedev and K. Kassner, Phys. Rev. E **72**, 056703 (2005).
[25] D. Medvedev, T. Fischaleck, and K. Kassner, Phys. Rev. E **74**, 031606 (2006).
[26] R. Rojas, T. Takaki, and M. Ohno, J. Comput. Phys. **298**, 29 (2015).
[27] M. Yang, S. M. Xiong, and Z. Guo, Acta Mater. **92**, 8 (2015).
[28] M. Yang, S. M. Xiong, and Z. Guo, Acta Mater. **112**, 261 (2016).
[29] J. C. Ramirez, C. Beckermann, A. Karma, and H. J. Diepers, Phys. Rev. E **69**, 051607 (2004).
[30] B. Echebarria, R. Folch, A. Karma, and M. Plapp, Phys. Rev. E **70**, 061604 (2004).
[31] R. Folch and M. Plapp, Phys. Rev. E **72**, 011602 (2005).
[32] J. Du, A. Zhang, Z. Guo, M. Yang, M. Li, and S. Xiong, ACS Omega **2**, 8803 (2017).
[33] S. G. Kim, W. T. Kim, T. Suzuki, and M. Ode, J. Cryst. Growth **261**, 135 (2004).
[34] L. Rátkai, A. Szállás, T. Pusztai, T. Mohri, and L. Gránásy, J. Chem. Phys. **142**, 154501 (2015).
[35] A. Zhang, Z. Guo, and S. M. Xiong, J. Appl. Phys. **121**, 125101 (2017).
[36] N. Moelans, B. Blanpain, and P. Wollants, CALPHAD **32**, 268 (2008).
[37] L. Chen, Annu. Rev. Mater. Res. **32**, 113 (2002).
[38] W. J. Boettinger, J. A. Warren, C. Beckermann, and A. Karma, Annu. Rev. Mater. Res. **32**, 163 (2002).
[39] A. Karma, Phys. Rev. Lett. **87**, 115701 (2001).
[40] M. Serefoglu, R. E. Napolitano, and M. Plapp, Phys. Rev. E **84**, 011614 (2011).
[41] A. Parisi and M. Plapp, EPL **90**, 26010 (2010).
[42] A. Parisi and M. Plapp, Acta Mater. **56**, 1348 (2008).
[43] J. Hötzer, M. Jainta, P. Steinmetz, B. Nestler, A. Dennstedt, A. Genau, M. Bauer, H. Köstler, and U. Rüde, Acta Mater. **93**, 194 (2015).
[44] J. Hötzer, P. Steinmetz, M. Jainta, S. Schulz, M. Kellner, B. Nestler, A. Genau, A. Dennstedt, M. Bauer, H. Köstler, and U. Rüde, Acta Mater. **106**, 249 (2016).
[45] Z. Guo and S. M. Xiong, Comput. Phys. Commun. **190**, 89 (2015).
[46] X. Zhang, J. Kang, Z. Guo, S. Xiong, and Q. Han, Comput. Phys. Commun. **223**, 18 (2018).
[47] D. Raabe, Modell. Simul. Mater. Sci. Eng. **12**, R13 (2004).
[48] P. L. Bhatnagar, E. P. Gross, and M. Krook, Phys. Rev. **94**, 511 (1954).
[49] S. Chen, H. Chen, D. Martinez, and W. Matthaeus, Phys. Rev. Lett. **67**, 3776 (1991).
[50] Y. H. Qian, D. D'Humières, and P. Lallemand, Europhys. Lett. **17**, 479 (1992).
[51] T. Takaki, R. Rojas, S. Sakane, M. Ohno, Y. Shibuta, T. Shimokawabe, and T. Aoki, J. Cryst. Growth **474**, 146 (2017).
[52] R. S. Maier, R. S. Bernard, and D. W. Grunau, Phys. Fluids **8**, 1788 (1996).
[53] M. Berger and I. Rigoutsos, IEEE Trans. Syst. Man Cybern. **21**, 1278 (1991).
[54] O. Filippova and D. Hänel, J. Comput. Phys. **147**, 219 (1998).
[55] O. Filippova and D. Hänel, J. Comput. Phys. **165**, 407 (2000).

[56] V. Datye and J. S. Langer, Phys. Rev. B **24**, 4155 (1981).
[57] W. Kurz and D. J. Fisher, *Fundamentals of Solidification* (Trans Tech Publications Ltd., Aedermannsdorf, Switzerland, 1992).
[58] J. Mergy, G. Faivre, C. Guthmann, and R. Mellet, J. Cryst. Growth **134**, 353 (1993).
[59] N. Maraşli and J. D. Hunt, Acta Mater. **44**, 1085 (1996).
[60] M. Gündüz and J. D. Hunt, Acta Mater. **33**, 1651 (1985).
[61] C. J. Vreeman, M. J. M. Krane, and F. P. Incropera, Int. J. Heat Mass Transfer **43**, 677 (2000).
[62] C. J. Vreeman and F. P. Incropera, Int. J. Heat Mass Transfer **43**, 687 (2000).
[63] J. D. Bozeman and C. Dalton, J. Comput. Phys. **12**, 348 (1973).
[64] U. Ghia, K. N. Ghia, and C. T. Shin, J. Comput. Phys. **48**, 387 (1982).
[65] R. Schreiber and H. B. Keller, J. Comput. Phys. **49**, 310 (1983).
[66] S. Hou, Q. Zou, S. Chen, G. Doolen, and A. Cogley, J. Comput. Phys. **118**, 329 (1994).
[67] R. A. Johnson and D. W. Wichern, *Applied Multivariate Statistical Analysis* (Pearson–Prentice Hall, Upper Saddle River, NJ, 2007).
[68] P. Magnin and R. Trivedi, Acta Metall. Mater. **39**, 453 (1991).